Supplementary Information

Substantially Enhanced Electric Potential of Confined Water via Dynamic Nanocurved Interfaces

Miao Wang[1,2†], Yu Liu[2†], Lejian Yu[1†], Shisheng Zheng[3†], Dan Tan[5†], Yaqi Hou[1,7], Xiao-Ting Wang[2], Zhong-zhang Shi[3], Yunmao Zhang[1,8], Bingwei Mao[1], Jian-Feng Li[3], Yao-Hui Wang[2]*, Zhong Lin Wang[4]*, Xu Hou[1,2,6]*

[1]Institute of Electrochemical Science and Engineering, State Key Laboratory of Physical Chemistry of Solid Surfaces, College of Chemistry and Chemical Engineering, Xiamen University, Xiamen 361005, P. R. China.

[2]The Higher Educational Key Laboratory for Biomedical Engineering of Fujian Province, Research Center of Biomedical Engineering of Xiamen, Department of Biomaterials, College of Materials, Xiamen University, Xiamen 361005, P. R. China.

[3]College of Energy, Xiamen University, Xiamen 361005, P. R. China.

[4]Beijing Institute of Nanoenergy and Nanosystems, Chinese Academy of Sciences, Beijing 101400, P. R. China.

[5]School of Advanced Materials and Nanotechnology, Xidian University, Xian 710126, P. R. China.

[6]College of Physical Science and Technology, Xiamen University, Xiamen 361005, P. R. China.

[7]Institute of Flexible Electronics (IFE, Future Technologies), Xiamen University, Xiamen 361102, Fujian, P. R. China.

[8]College of Materials Science and Engineering, Huaqiao University, Xiamen, 361021, P. R. China.

*Corresponding author. Email: houx@xmu.edu.cn; zlwang@binn.cas.cn; yaohuiwang@xmu.edu.cn

†These authors contributed equally to this work.

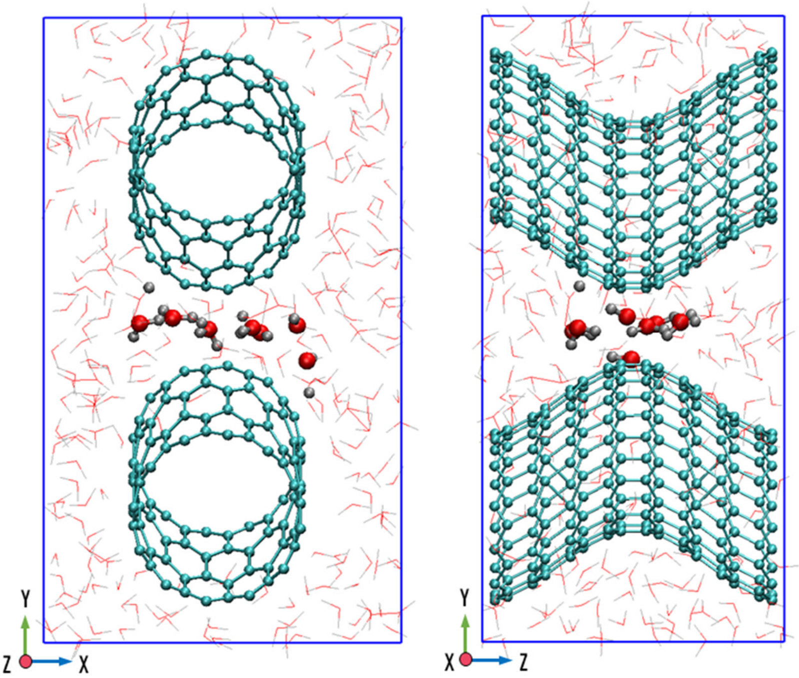

Supplementary Fig. 1 | Constructed model of the convex surface of CNTs from top view and side view.

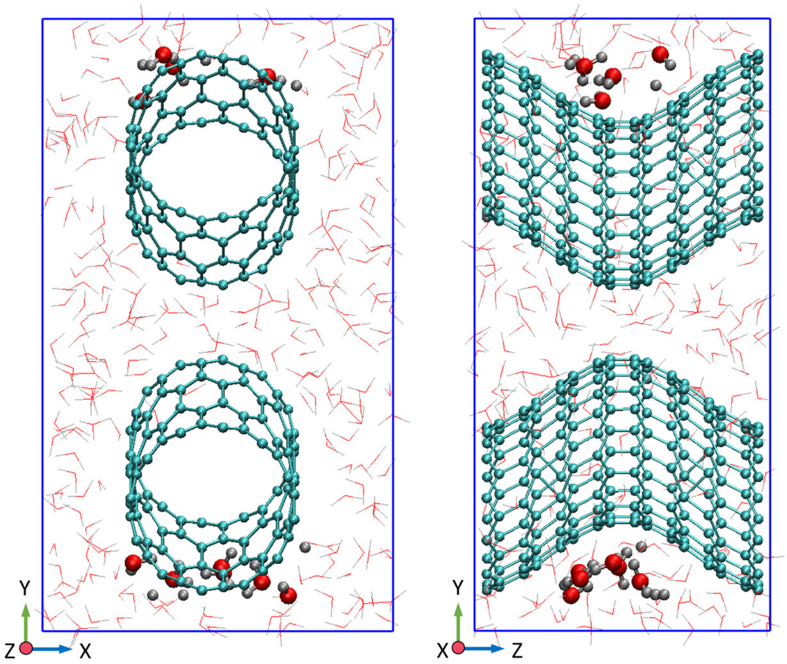

Supplementary Fig. 2 | Constructed model of the concave surface of CNTs from top view and side view.

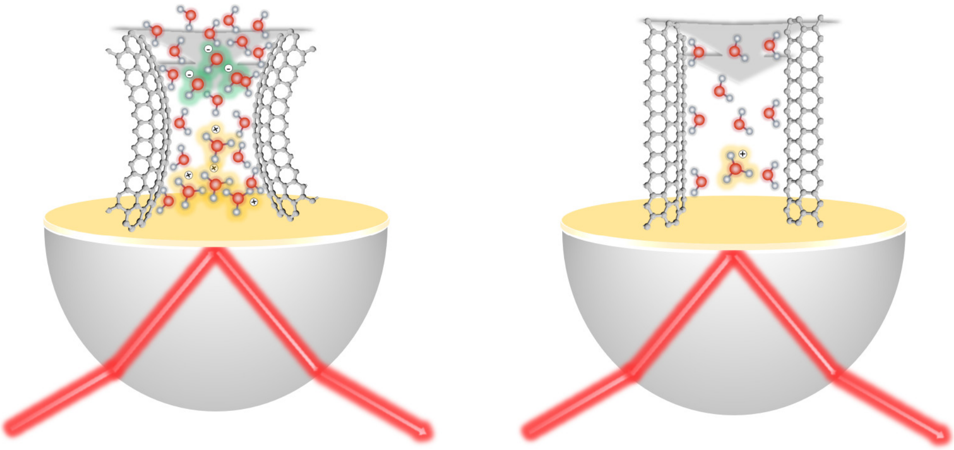

Supplementary Fig. 3 | The characterization was performed using in-situ attenuated total reflection surface-enhanced infrared spectroscopy (ATR-SEIRAS): a rough gold film (~50 nm) was chemically deposited onto a silicon substrate (infrared window) to amplify the interfacial infrared signals. Planar and curved CNTs were then pressed onto the gold film surface to achieve seamless contact. Subsequently, humidified argon gas and water vapor were introduced, and time-resolved infrared spectra were collected simultaneously.

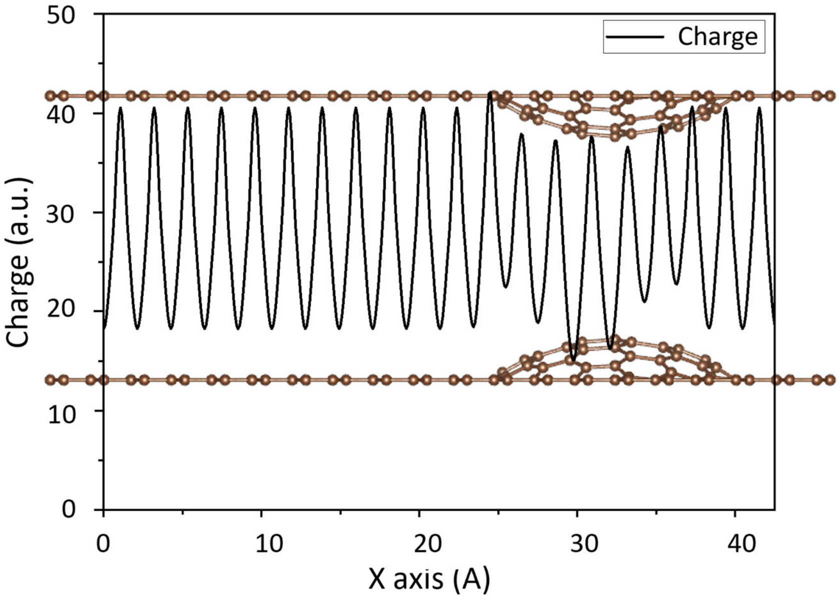

Supplementary Fig. 4 | Curved graphene electron density map. From the bent graphene electron diagram, the charge content in the curved part of graphene is less than that in the flat part, which can be regarded as a relatively positive charge region and has a selective screening effect on cations and anions.

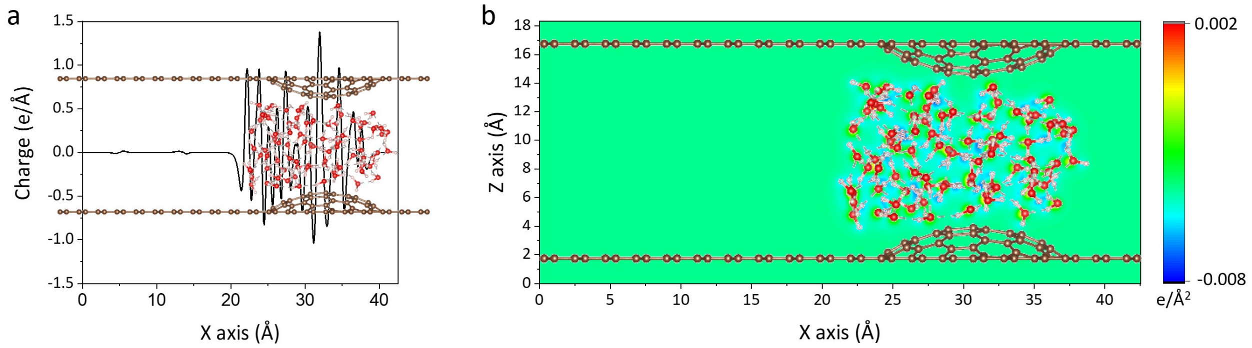

Supplementary Fig. 5 | Electron density difference map of pure water model when most of the water molecules accumulate on the curved graphene surface. a, The projection of electron density in the x-axis direction. **b,** The projection of electron density on the ZOX plane.

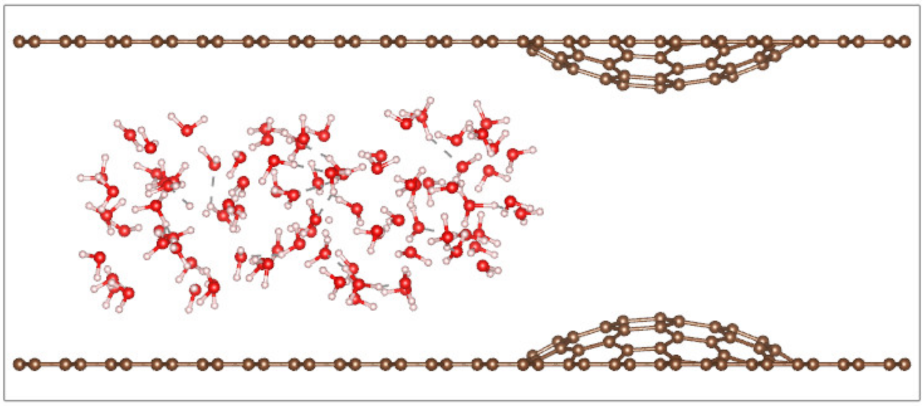

Supplementary Fig. 6 | The picture of pre-optimized hydronium ion model.

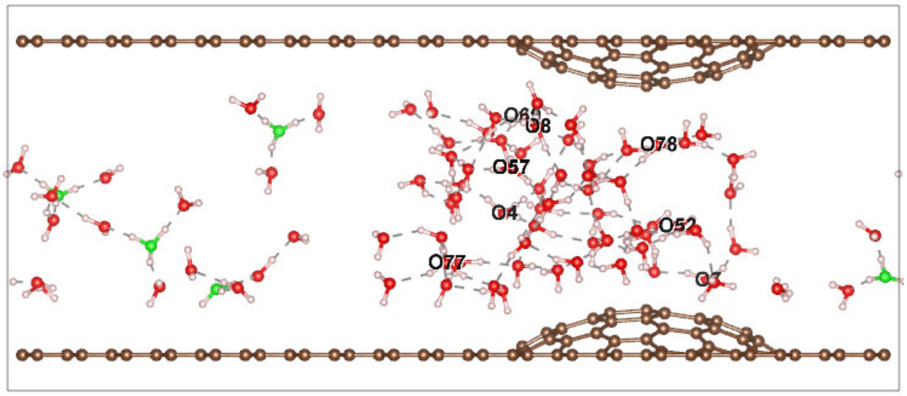

Supplementary Fig. 7 | Distribution of hydronium ion when most water molecules accumulate on the curved graphene surface. Green oxygen atoms are marked as passing through, and oxygen atoms with numbers are marked as not passing through.

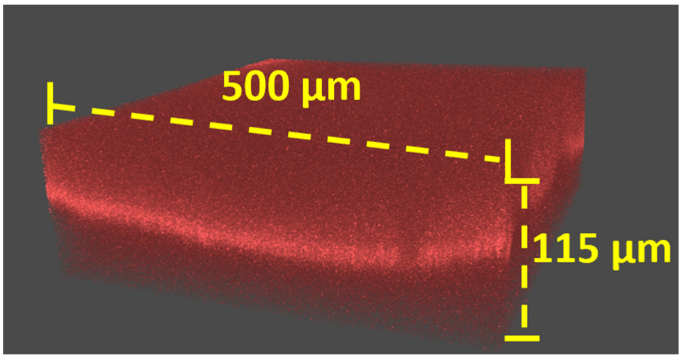

Supplementary Fig. 8 | Fluorescence confocal images of the CNTs after layer-by-layer self-assembly using PSS and PAH polyelectrolyte.

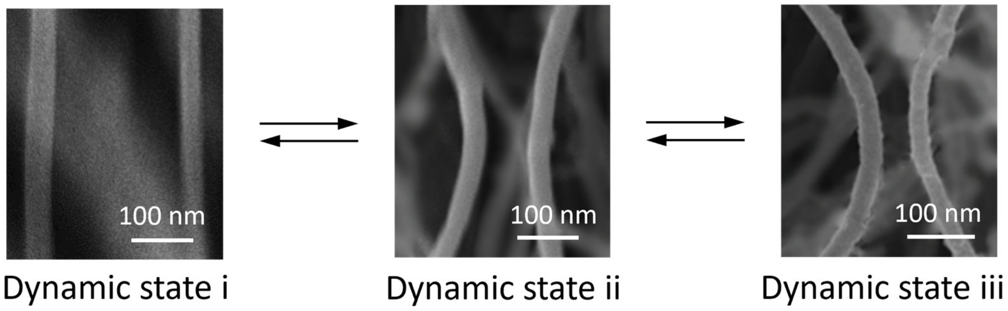

Supplementary Fig. 9 | The SEM images at high magnifications from dynamic state i to iii, indicating the confinement of adjacent CNTs.

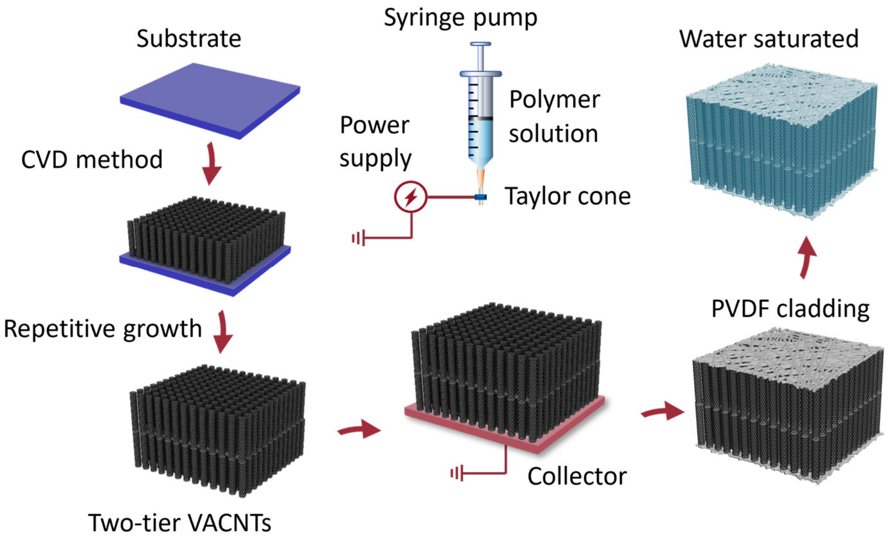

Supplementary Fig. 10 | Electrospun method to fabricate the PVDF coated on both sides of the two-tier CNT arrays prepared by the FCCVD method. The obtained PVDF/CNTs/PVDF sandwich film (PCP) was then saturated with pure water.

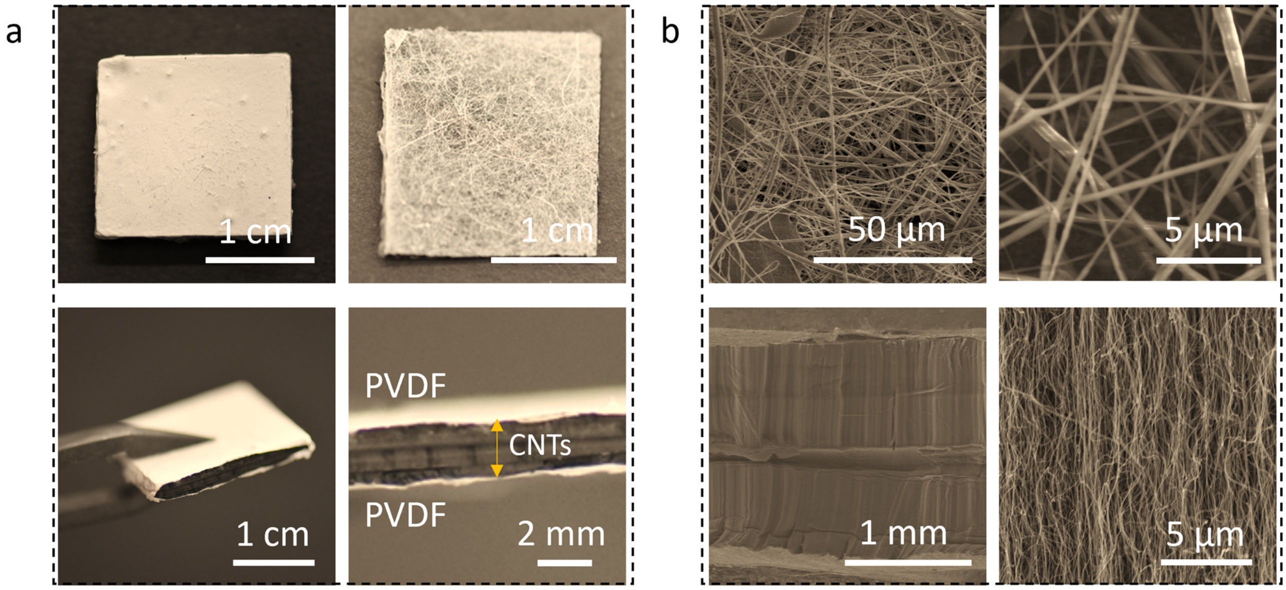

Supplementary Fig. 11 | The optical and SEM images of PCP. a, Upper: Optical images of PVDF on both top and bottom sides of CNTs. Lower: Optical images of the side view of a two-tier PCP. **b,** SEM images of PVDF (upper) on surfaces of PCP and side view of two-tier CNT arrays (lower) inside PCP. The right images show an enlarged view of the left image.

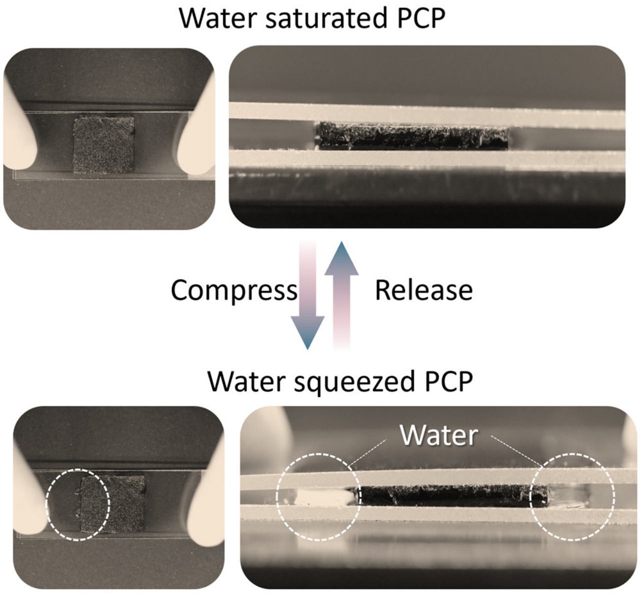

Supplementary Fig. 12 | Photograph of the water saturated PCP under compressed and water release process.

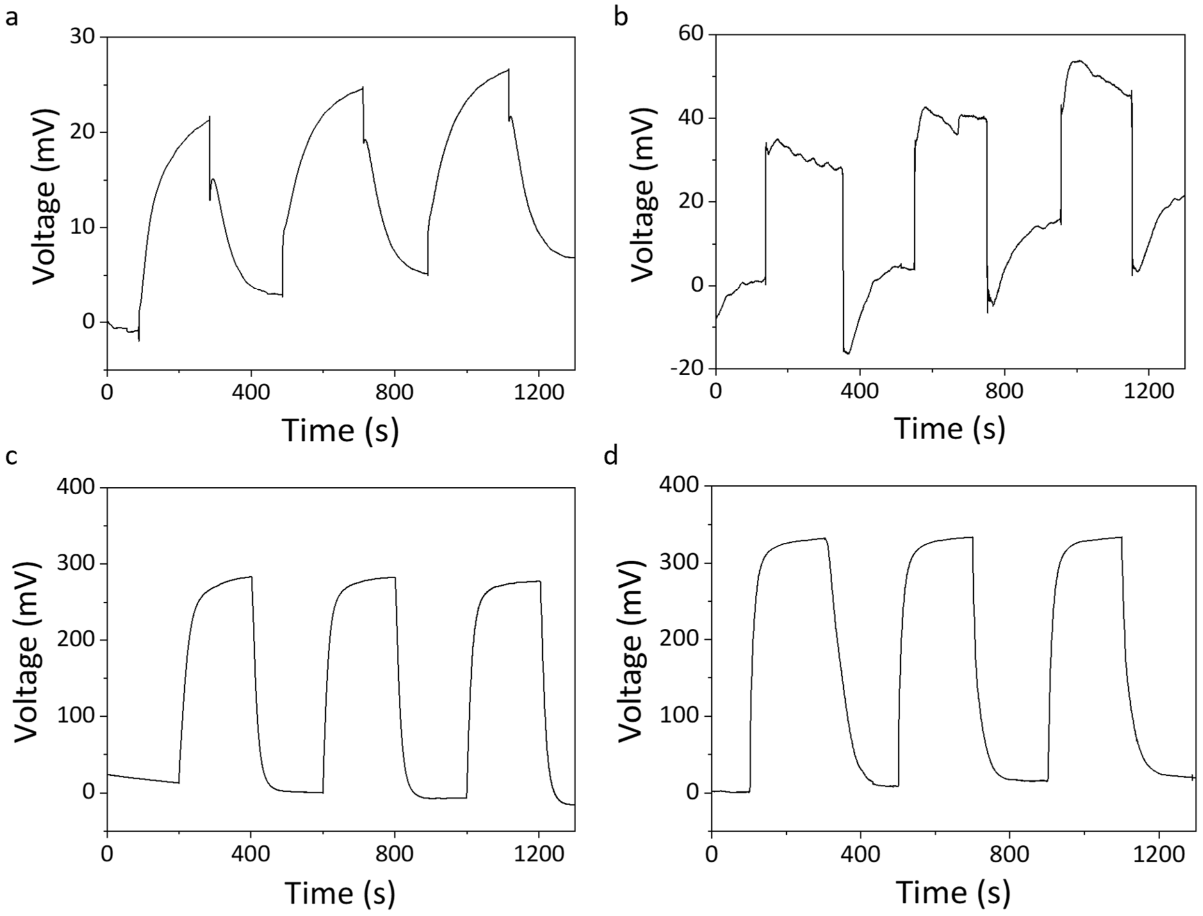

Supplementary Fig. 13 | The influence of CNTs structure on CPE generation under water flow. The open-circuit voltage of **a,** pure disordered CNTs, **b,** PCP with disordered CNTs, **c,** pure ordered CNTs, and **d,** PCP with ordered CNTs. All mentioned above were immersed in flowing water with a velocity of 0.5 mL·min^{-1}.

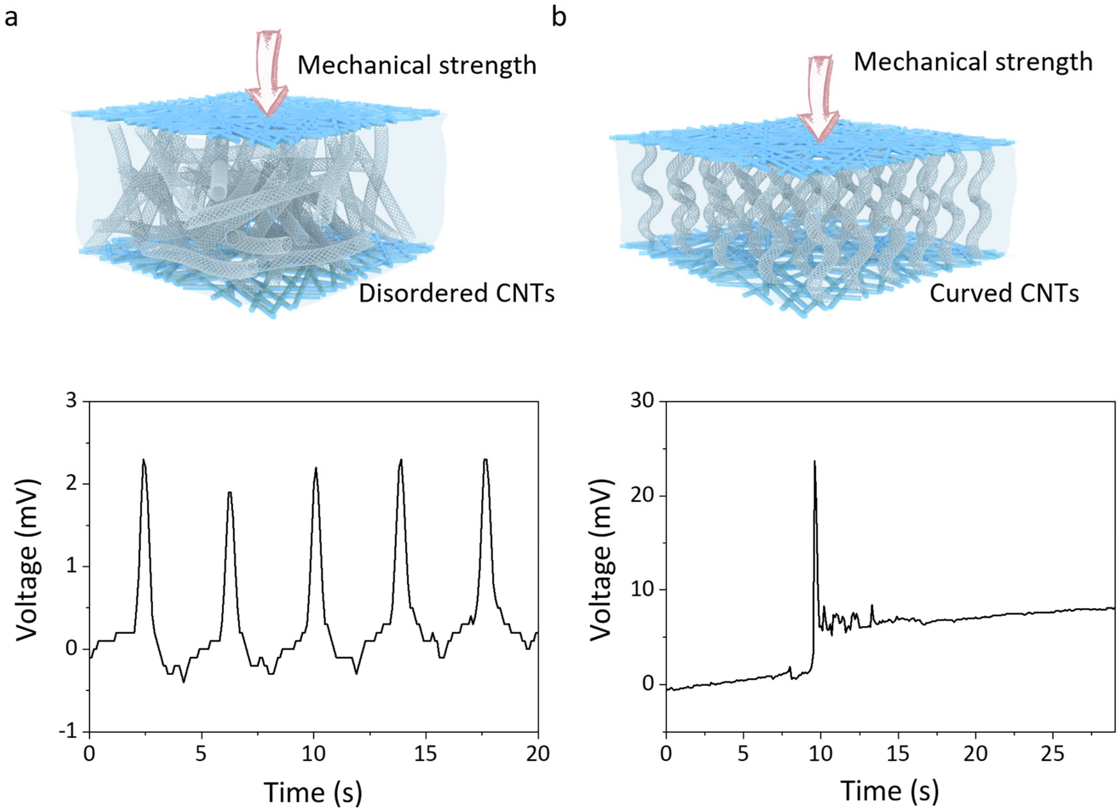

Supplementary Fig. 14 | The open-circuit voltage of different CNTs structure in static water. a, Disordered CNTs coated with PVDF undergoing compression at a thickness of 2 mm. **b,** Ordered and curved CNTs coated with PVDF undergoing compression at a thickness of 2 mm.

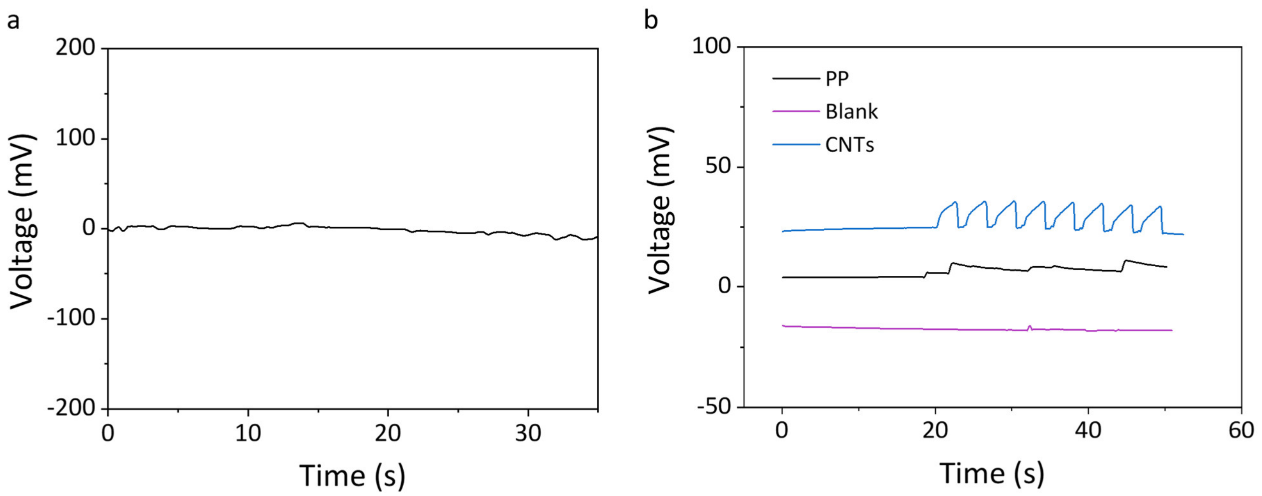

Supplementary Fig. 15 | Control experiment comparing the open circuit voltage in different conditions. a, The open circuit voltage of the PCP in the water-free state. The curve indicates that the absence of water results in zero output voltage. **b,** Open circuit voltage of the blank control experiment with polypropylene (PP) membrane, and the water substituted CNTs. The blank control curve shows no potential difference, effectively eliminating any interference from the instrument or experimental procedure. Similarly, the pure PP membrane fails to generate a consistent potential difference. In contrast, only the water-absorbing CNTs produce a distinct, regular potential difference peak during compression and recovery, clearly indicating that the mechanism involves an interaction between water and CNTs.

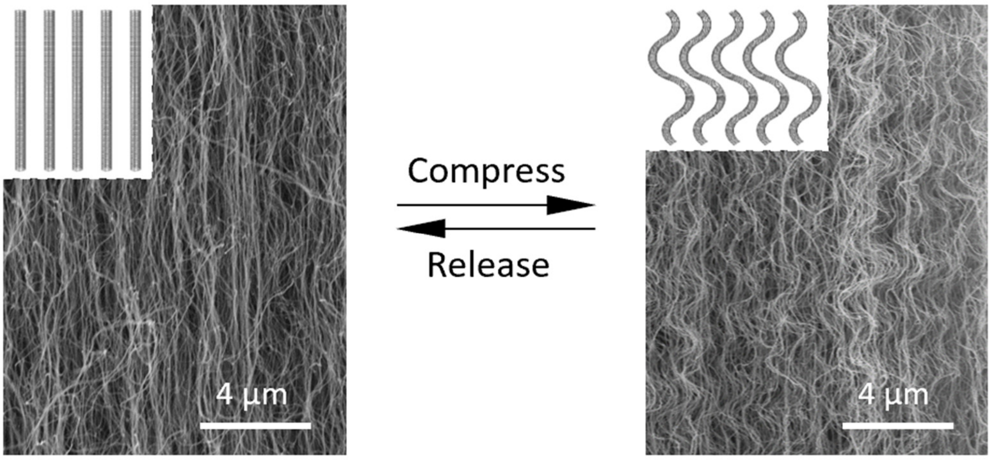

Supplementary Fig. 16 | Cross-section SEM images of the dynamic conversion behaviors of CNT arrays under external mechanical strength.

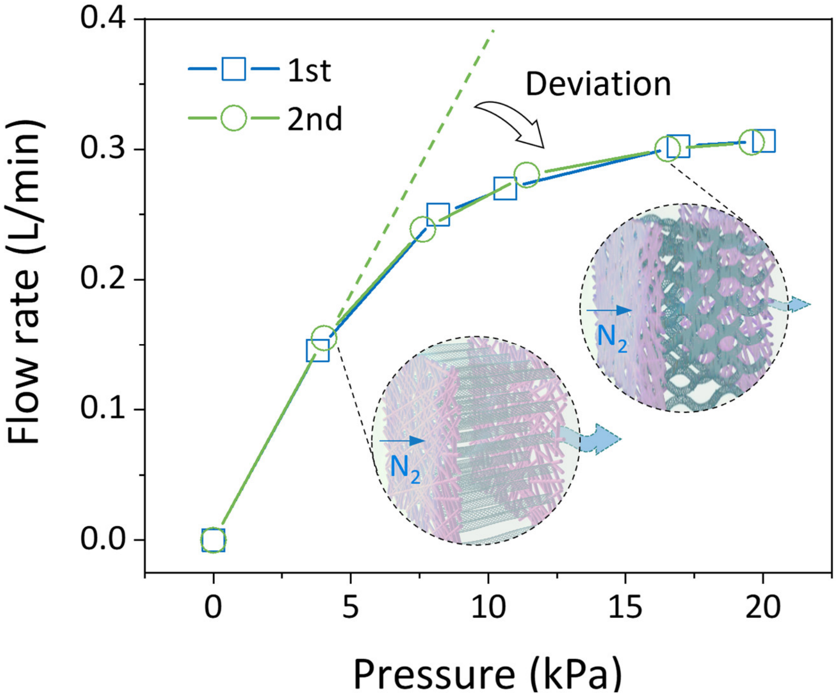

Supplementary Fig. 17 | The flow rate variation as a function of the applied nitrogen gas pressure. Arise in the transmembrane pressure would increase the flow rate on the basis of Darcy's law, indicating the good gas permeability of CNTs.

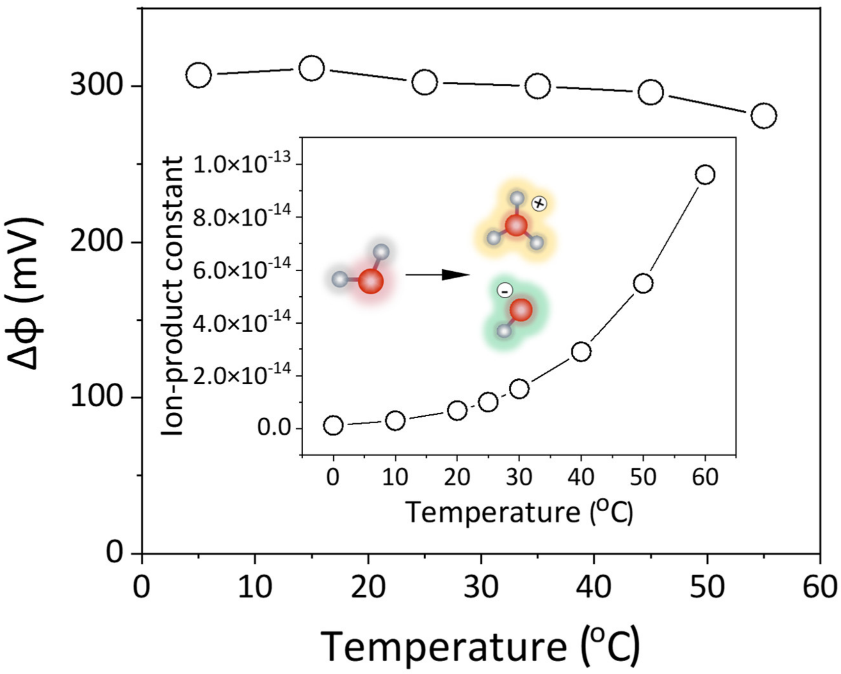

Supplementary Fig. 18 | The output CPE variation as a function of the ambient environment temperature at 0.5 mL·min^{-1}. The inset is the change of the dissociation constant of water with temperature. This result indicates the temperature has no significant effect on the CPEs owing to the equivalent quantity of hydronium and hydroxide under different temperatures.

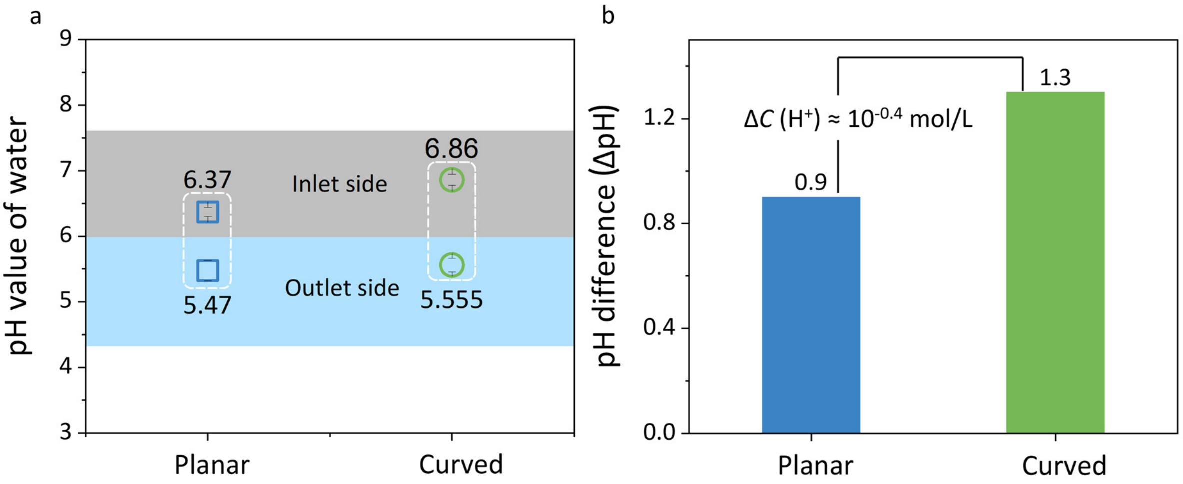

Supplementary Fig. 19 | Real-time pH measurements and hydronium concentration difference in PCP under planar and curved states. a, The real-time pH value of water from the inlet side and outlet side when measuring the CPEs of PCP under planar and curved states. **b,** The pH difference between the planar state and curved state, showing that the hydronium concentration difference can reach $10^{-0.4}$ mol·L^{-1}.

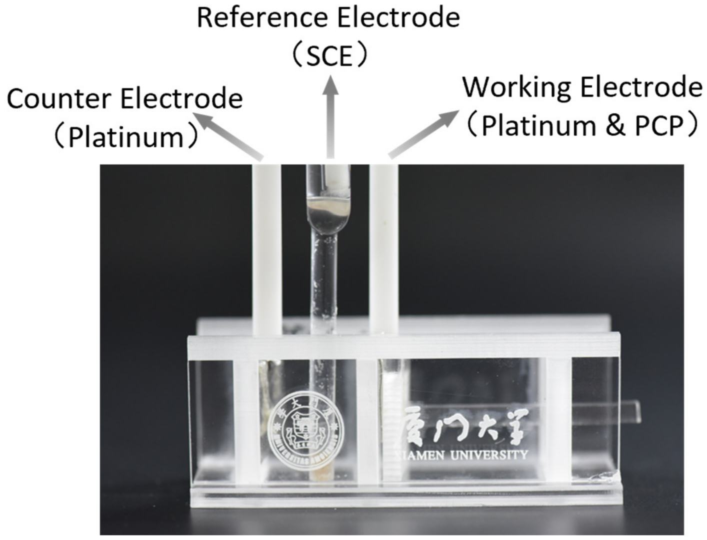

Supplementary Fig. 20 | The optical photograph of a homemade power generation device showing the assembly for CPEs generation in a standard three-electrode system.

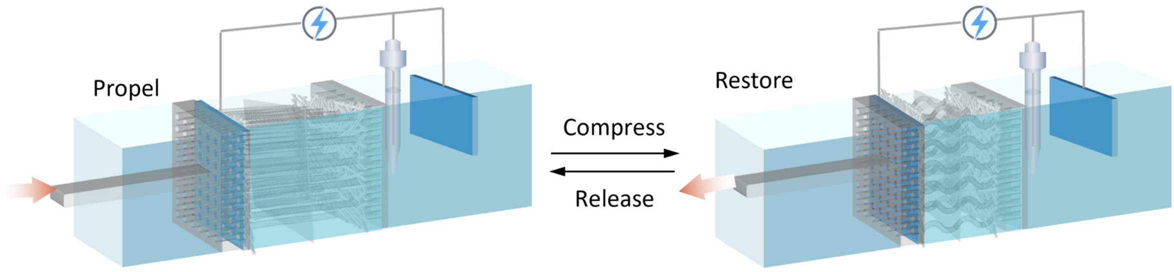

Supplementary Fig. 21 | Schematic illustration of the dynamic process for measuring the induced CPEs.

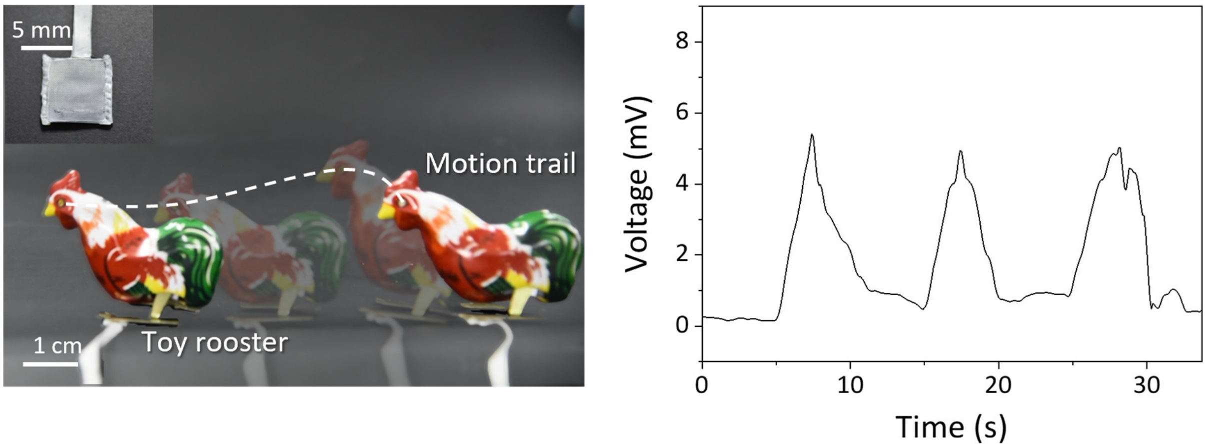

Supplementary Fig. 22 | Motion pressure sensing application of the PCP. The dependence of open-circuit voltage on time when the toy rooster was in motion.

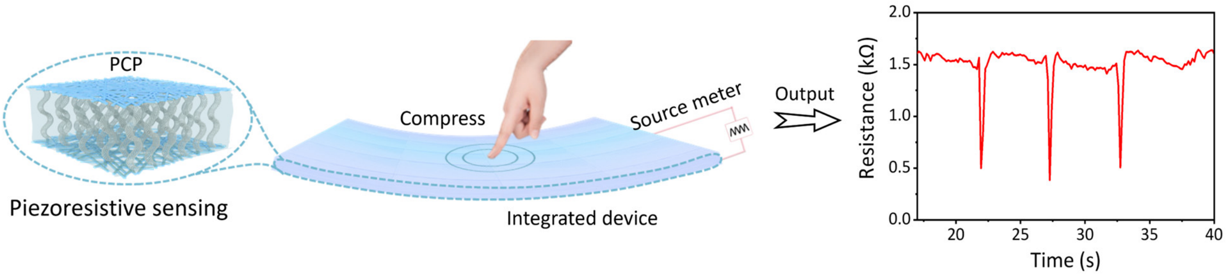

Supplementary Fig. 23 | Piezoresistive sensing based on the change in resistance with time during repeated compression/recovery (the left side is the schematic illustration).

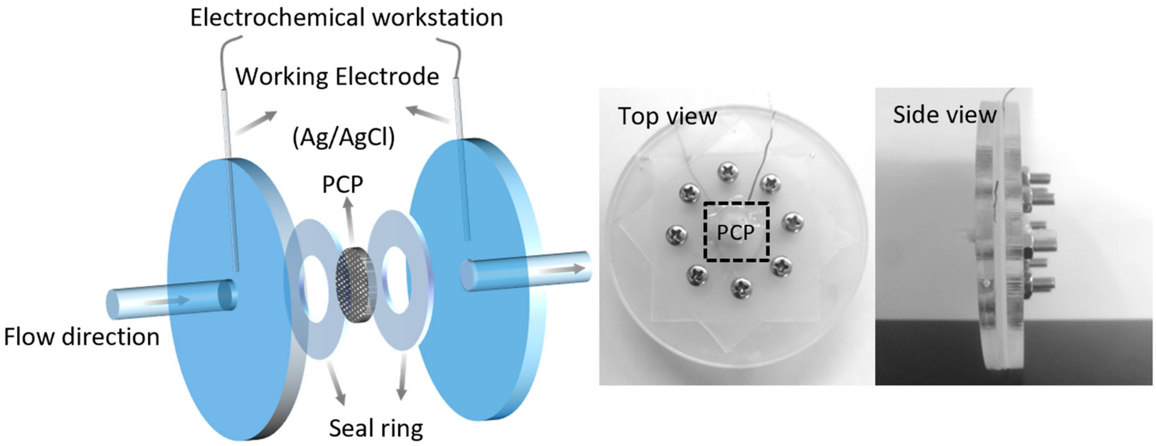

Supplementary Fig. 24 | The illustration and optical photographs of the customized assembly a two-electrode device for water flow detection. The outer diameter of the pipeline is 4 mm.

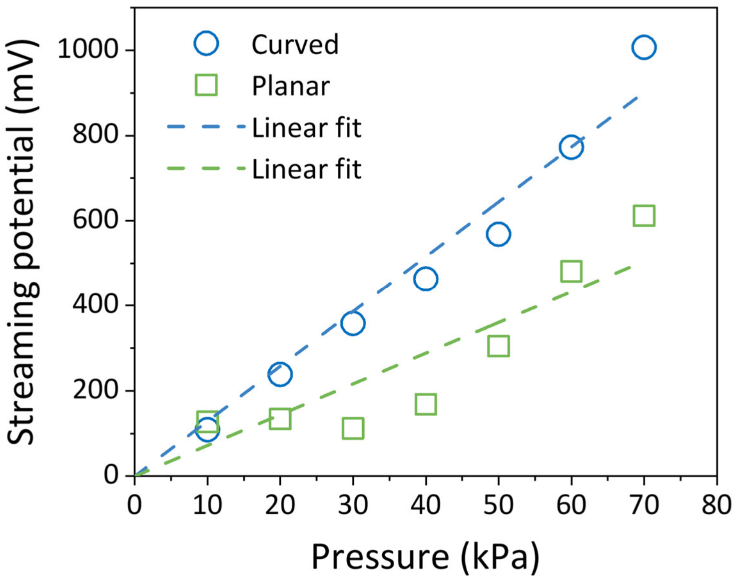

Supplementary Fig. 25 | The streaming potential variation as a function of the applied pressure under planar and curved states.

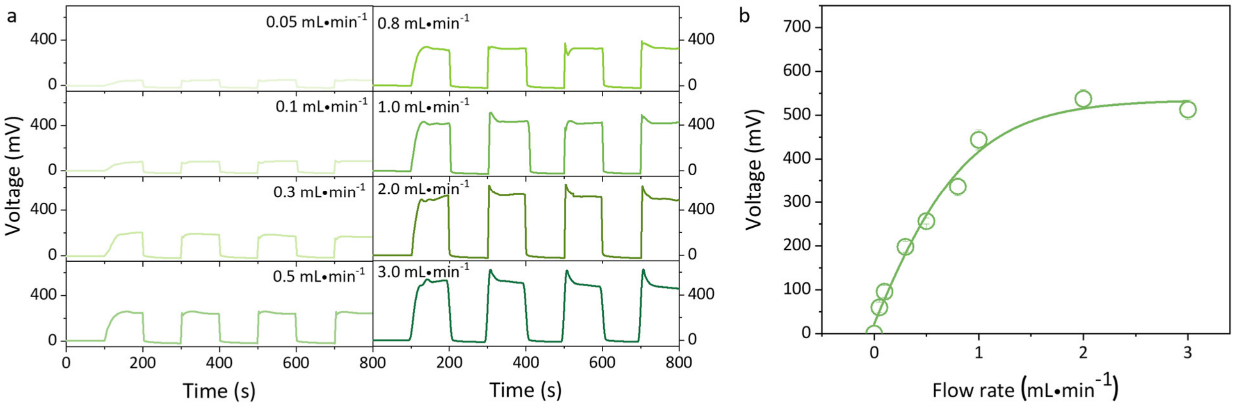

Supplementary Fig. 26 | Control experiment on streaming potential output with anodic aluminum oxide (AAO). a, The output streaming potential measured in the commercial AAO at different water flow rates. **b,** The relationship between the measured streaming potential and flow rates with velocity of 0.05, 0.1, 0.3, 0.5, 0.8, 1.0, 2.0, and 3.0 mL·min^{-1}.

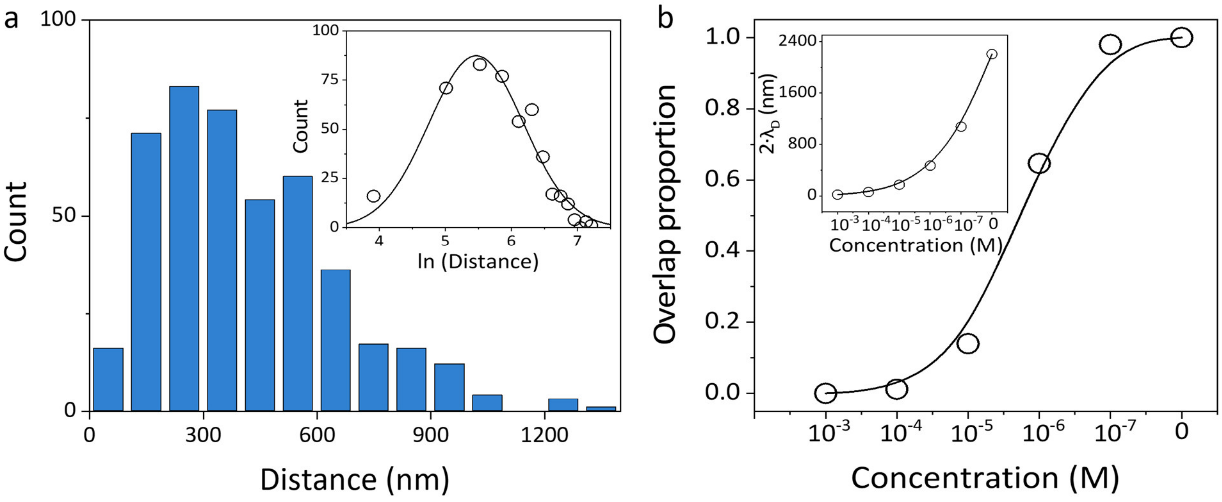

Supplementary Fig. 27 | The statistical analysis of CNT arrays and their electrical double layers (EDLs). a, Statistical distribution of the distance (served as the effective diameter of the inter nanochannels) between CNT arrays analyzed from the numerous SEM images. The inset manifests the ln fitting result of the distribution based on a normal distribution $f(x) = a \cdot \exp\left(-((x-b)/c)^2\right)$. **b,** The EDLs overlap proportion of distribution under different concentrations of KCl solutions. The inserted curve shows twice the length of Debye length in different concentrations of KCl solutions, which represents the critical distance for the EDLs to overlap under different concentrations.

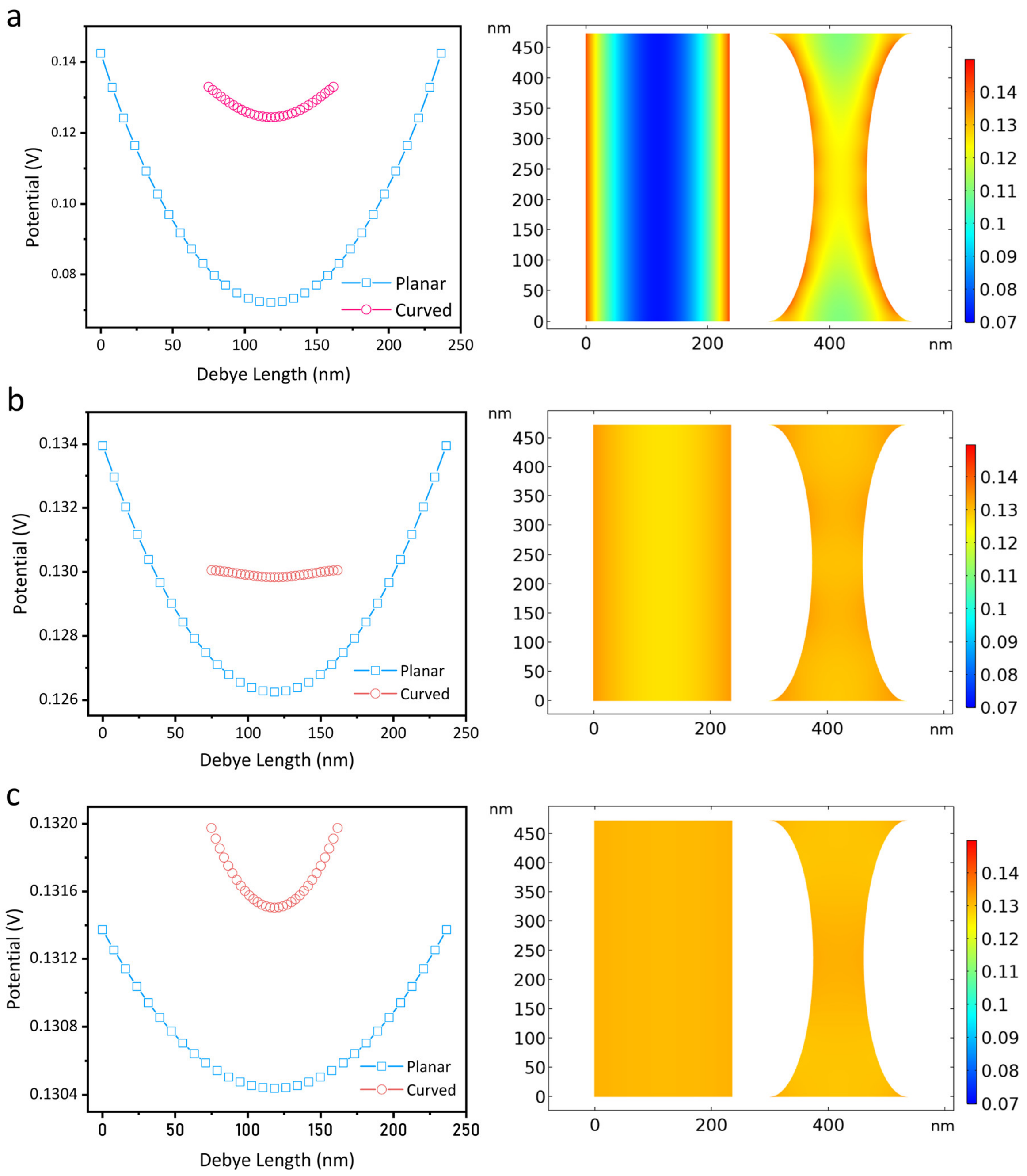

Supplementary Fig. 28 | The potential output distributions under a range of Debye length with a, water, b, 0.0001 mM KCl solution, and c, 0.001 mM KCl solution based on finite element method simulated using COMSOL Multiphysics® software. The blue curves denote the planar state, and the red curves represent the curved state.

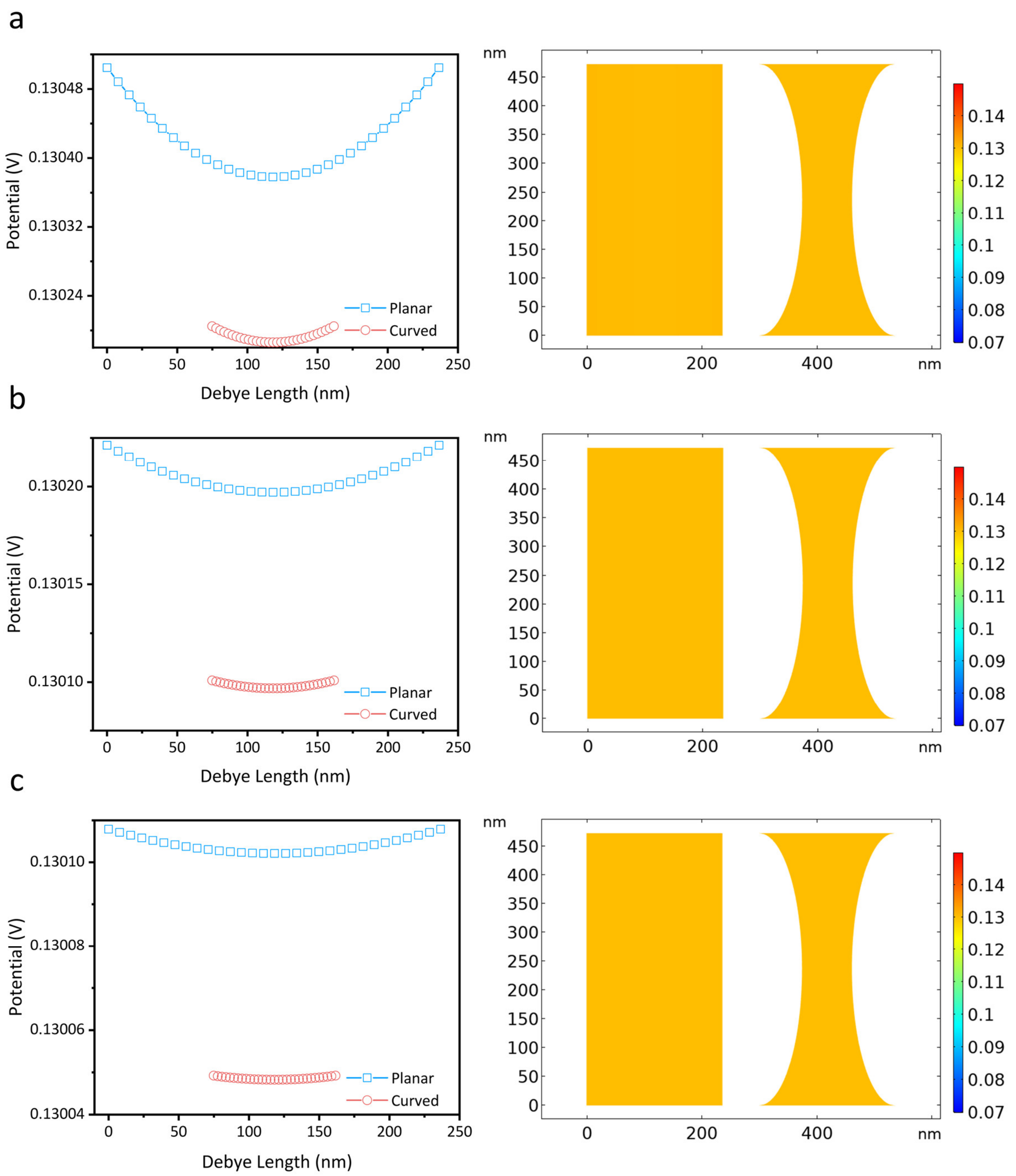

Supplementary Fig. 29 | The potential output distributions under a range of Debye length with gradient concentrations of a, 0.01 mM KCl, b, 0.1 mM KCl, and c, 1 mM KCl solutions based on finite element method simulated using COMSOL Multiphysics® software. The blue curves denote the planar state, and the red curves represent the curved state.

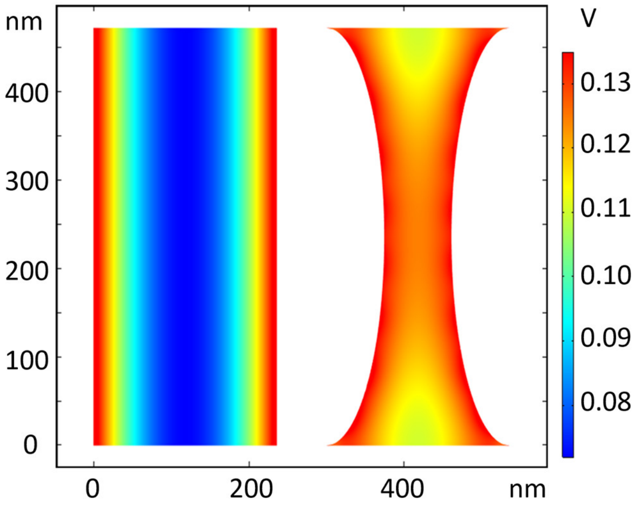

Supplementary Fig. 30 | The diagram of the calculated electrical potential distribution profile in water, simulated using COMSOL Multiphysics® software.

Supplementary Table 1 | Debye length under different water/electrolyte solutions with gradient concentrations.

Electrolyte solution	KCl solution					Water
	10^{-3} mM	10^{-4} mM	10^{-5} mM	10^{-6} mM	10^{-7} mM	
pH	5.77	5.69	5.64	6.18	6.66	7.12
Cation concentration (M)	1.002×10^{-3}	1.02×10^{-4}	1.23×10^{-5}	1.66×10^{-6}	3.19×10^{-7}	7.586×10^{-8}
λ_D (nm)	9.605	30.094	86.713	235.901	538.432	1103.760
$2\cdot\lambda_D$ (nm)	19.210	60.188	173.426	471.802	1076.864	2207.520

Supplementary Table 2 | The potential output distributions under a range of Debye length with gradient concentrations of KCl solutions/water based on the finite element method simulated using COMSOL Multiphysics® software.

Electrolyte solution (mM)	Cation concentration (M)	λ_D (nm)	Planar potential (V)	Curved potential (V)
KCl solution 10^{-3}	1.002×10^{-3}	9.605	0.072	0.124
KCl solution 10^{-4}	1.02×10^{-4}	30.094	0.126	0.129
KCl solution 10^{-5}	1.23×10^{-5}	86.713	0.130	0.131
KCl solution 10^{-6}	1.66×10^{-6}	235.901	0.130	0.130
KCl solution 10^{-7}	3.19×10^{-7}	538.432	0.130	0.130
Water	7.586×10^{-8}	1103.760	0.130	0.130